International Journal of Computational Methods
(2026) 2650035 (26 pages)
© World Scientific Publishing Company
DOI: 10.1142/S0219876226500350

World Scientific
www.worldscientific.com

Annular and Disk Finite Elements for Two-Dimensional Elastostatic Problems

Hui Pan and Yijun Liu*

Department of Mechanics and Aerospace Engineering
Southern University of Science and Technology
1088 Xueyuan Avenue, Nanshan District
Shenzhen, Guangdong, P. R. China
**liuyj3@sustech.edu.cn*

Received 23 June 2025
Revised 10 February 2026
Accepted 20 April 2026
Published 19 May 2026

Modeling materials and microstructures composed of circular particles using standard finite elements poses a dual challenge: the polynomial-based geometric mapping introduces discretization errors on curved boundaries, and the large number of internal degrees of freedom required for each particle creates a computational bottleneck. This paper presents a new annular finite element and a circular disk super element to address both issues for two-dimensional (2D) elastostatic problems. The annular element employs an exact analytical geometric mapping based on polar coordinates, while the displacement field is interpolated using standard 8-node quadrilateral shape functions to maintain compatibility with conventional finite element frameworks. A disk super element is further constructed by applying static condensation to eliminate internal degrees of freedom. Convergence studies confirm that the annular element achieves optimal convergence rates, consistent with those of the standard isoparametric counterpart, while providing exact geometric fidelity on circular boundaries. Additional benchmarks involving stress concentrations and concentrated loads validate the element's accuracy. The efficiency and physical consistency of the disk super element are demonstrated through disk packing simulations, where the effective Young's modulus converges with increasing number of disks, showing the method's potential for homogenization analysis of particulate composites.

Keywords: Annular element; disk super element; 2D elastostatic problems.

1. Introduction

There are many materials or microstructures that are made of particles such as various particulate or granular composites, three-dimensional (3D) printed materials or microstructures and so on (see Giovine *et al.* [2020] for a special issue of IJSS on granular materials). Usually, these particles are of circular or spherical shapes.

*Corresponding author.

In addition, structures can be formed by using circle packing [Stephenson (2003)] within an area or using sphere packing within a volume. To study the mechanical properties of such materials or structures, numerical methods are essential. While Discrete Element Method (DEM) is widely adopted for simulating granular flows and large-scale particle dynamics [Chen *et al.* (2022); Liu *et al.* (2023); Fransen *et al.* (2026)], and Multi-Particle Finite Element Method (MPFEM) has been developed for high-density compaction processes [Yuan *et al.* (2025)], detailed stress analysis within the continuum often requires the Finite Element Method (FEM). Concurrent multi-scale approaches coupling DEM and FEM have also been proposed to bridge these regimes [Mathews *et al.* (2026)]. However, applying the finite elements in a primitive way to model each circle or sphere with many elements will be inefficient computationally and quickly beyond the reach, when the number of circles or spheres increases. Therefore, a better or special type of finite elements for modeling particulate materials, and eventually modeling 3D printed materials and microstructure, is needed. As a starting point, studying 2D models of such problems, and developing an efficient, yet accurate, 2D annular element and circular disk element will be necessary and an important first step.

The mechanical analysis of materials and structures containing circular or spherical inclusions is indeed a fundamental problem in computational mechanics. Such microstructures are ubiquitous in nature and engineering, ranging from granular soils and rocks in geomechanics [Zhao (2020); Liu *et al.* (2021)] to particle-reinforced composite materials [Wang *et al.* (2018); Zhang and Wang (2019)]. More recently, with the advent of additive manufacturing, cellular structures and lattice materials usually involving circular struts or curved boundaries are becoming increasingly important [Ngo *et al.* (2018)]. Understanding the stress distribution and interaction between these circular domains is critical for predicting the effective properties and failure mechanisms of the macroscopic system.

Numerical methods, particularly the FEM, have been the dominant tool for such analyses. However, modeling circular geometries using traditional finite elements (e.g., triangles or quadrilaterals with straight edges) presents significant challenges. To capture the curvature of a circle boundary accurately, a very fine mesh is typically required, which leads to a substantial increase in the computational cost [Marussig and Hughes (2018)]. Even with refined meshes, the geometric approximation error — known as the geometric discretization error — cannot be completely eliminated, leading to stress concentration inaccuracies at the boundaries [Sevilla and Huerta (2018)]. In recent years, advanced numerical schemes such as the Isogeometric Analysis (IGA) have been proposed to resolve geometry issues by using NURBS basis functions [Xu *et al.* (2018)]. The Virtual Element Method (VEM) [Beirão da Veiga *et al.* (2019)] and Polygonal Finite Element Methods (PFEMs) [Chi and Paulino (2019)] also allow for better approximation of curved boundaries. Another alternative is the Scaled Boundary Finite Element Method (SBFEM) [Ooi *et al.* (2018)], which utilizes semi-analytical solutions.

Among these methods, IGA shares the most conceptual similarity with the present work, as both aim to integrate exact geometry into the numerical analysis. Recent developments in IGA have focused on handling trimmed geometries and multipatch coupling for complex engineering structures [Reichle *et al.* (2023); Guarino *et al.* (2024)]. However, despite its theoretical elegance and robustness [Jonsson *et al.* (2025)], the implementation of IGA within standard FEM frameworks remains nontrivial, often requiring significant changes to the code architecture. Historically, annular or sector elements were utilized around 1970 for circular plates [Raju and Rao (1969); Olson and Lindberg (1970); Sawko and Merriman (1971); Singh and Ramaswamy (1972); Raju *et al.* (1973); Wilson and Kirkhope (1976); Rao *et al.* (1977)]. While they offered geometric advantages, they fell out of favor as general parametric isoparametric elements became the dominant standard. However, a gap remains for specific modern applications involving dense assemblies of circular objects, typical of granular composites and microstructures. Commercial software packages effectively employ isoparametric polynomial elements. While robust, they face a dual challenge in this context: they inherently approximate the circular geometry (introducing geometric errors detrimental to contact analysis) and require excessive internal degrees of freedom (DOFs) to resolve stress gradients, creating a computational bottleneck for large-scale simulations. To address these challenges, we revisit the annular element concept, but enhanced with the "Super Element" technique. By leveraging the specific geometric regularities of the problem domain, we construct specialized elements that are both geometrically exact and computationally efficient via static condensation.

In this work, we present a new annular element and a circular disk super element for modeling 2D elastostatic problems. The proposed method distinguishes itself from existing approaches in two key aspects:

Geometric Exactness: Unlike standard isoparametric elements where geometry is interpolated via shape functions, the proposed element utilizes an analytical geometric mapping. The coordinates and their derivatives with respect to the parameter space are calculated exactly and simply. This ensures an exact representation of circular boundaries regardless of mesh size, eliminating geometric discretization errors — a critical advantage for contact mechanics and stress concentration analysis.

Computational Efficiency via Static Condensation: The disk super element utilizes substructuring techniques to condense internal DOFs. This allows for the high-fidelity modeling of individual particles with detailed internal meshes while maintaining a minimal DOF count for the global system. Moreover, for systems with identical disks — a common scenario in granular mechanics — the condensed stiffness matrix needs to be computed only once and reused for all instances, drastically reducing assembly time. In disk packing configurations, the structure is assembled by enforcing displacement compatibility at the tangential contact points between disks. This mechanism effectively facilitates stress transfer throughout

the granular system and ensures the positive definiteness of the global stiffness matrix.

The developed method and code are verified extensively through a systematic sequence of benchmark problems. First, the reliability of the annular element is rigorously established by comparing it with standard 8-node isoparametric quadrilateral elements (Q8) in the classic thick-walled cylinder problem. Second, its capability to capture severe stress gradients is demonstrated through the analysis of a circular disk with a small hole. Third, the method's robustness in handling singularities is validated using a disk subjected to concentrated diametrical forces. Finally, the computational efficiency and macroscopic consistency of the disk super element are showcased in large-scale disk packing simulations, confirming its potential for homogenization analysis of particulate composites.

The rest of this paper is organized as follows. In Sec. 2, the formulation of the new annular element is presented first, then the disk super element formulation is reviewed. In Sec. 3, numerical examples are presented to verify the developed elements and demonstrate the potential applications. In Sec. 4, some discussions are provided to conclude the paper.

2. Formulations

2.1. *Annular element formulation*

Distinct from the classical isoparametric element theory, the proposed annular element adopts a hybrid strategy that integrates analytical geometric mappings with standard parametric interpolation. Unlike standard isoparametric elements where geometric approximation errors may arise from polynomial mapping of curved boundaries, or sub-/super-parametric elements that primarily differ in polynomial order, the present formulation explicitly decouples the geometric description from the displacement field.

This hybrid formulation integrates two distinct components:

- **Exact Geometric Mapping:** As detailed in Sec. 2.1.1, the geometry is constructed via a composite mapping strategy: the transformation between the physical Cartesian coordinate system and the intermediate polar coordinate system is exact and analytical (see (2)), while the mapping from the natural reference system to the polar system utilizes linear interpolation (see (1)). This ensures exact representation of circular boundaries regardless of mesh size.
- **Standard Physical Interpolation:** As described in Sec. 2.1.2, the displacement field employs the standard 8-node quadrilateral (Q8) shape functions to maintain computational efficiency and compatibility.

This strategy allows for the precise modeling of circular domains with coarse meshes, eliminating geometric discretization errors while retaining the versatility of the FEM.

2.1.1. *Geometric description*

The annular element model to be devised is shown in Fig. 1, where the annular element (Fig. 1(b)) is a part from the whole annular plane (Fig. 1(a)). Eight nodes are used for the annular element, as shown in Fig. 1(b), where nodes 1 to 4 are the corner nodes numbered in a counterclockwise direction, and nodes 5 to 8 are the mid-side nodes also numbered counterclockwise. The annular domain for the element can be mapped to a standard square (Fig. 1(c)) using shape functions of the 8-node quadrilateral element.

To achieve an exact geometric representation, the formulation employs a composite mapping strategy involving three coordinate systems: the local natural system (ξ, η) for numerical integration, an intermediate polar system (r, θ) to capture the curvature, and the global Cartesian system (x, y) for the physical domain. The geometric mapping is thus constructed by transforming (ξ, η) first to (r, θ) and subsequently to (x, y).

The geometric mapping is implemented in two sequential stages to bridge the reference domain and the physical domain.

The first stage establishes the mapping $(\xi, \eta) \to (r, \theta)$ from the natural coordinate system to the intermediate polar coordinate system. This mapping step exploits the separable nature of the annular sector geometry, employing linear interpolation for the radial and angular coordinates independently:

$$\begin{cases} r(\xi, \eta) = \dfrac{1}{2}(1-\xi)\, r_1 + \dfrac{1}{2}(1+\xi)\, r_2, \\ \theta(\xi, \eta) = \dfrac{1}{2}(1-\eta)\, \theta_1 + \dfrac{1}{2}(1+\eta)\, \theta_2, \end{cases} \tag{1}$$

where r_1, r_2 are the inner and outer radii, and θ_1, θ_2 are the bounding angles of the element (see Fig. 1(b)).

The second stage performs the transformation $(r, \theta) \to (x, y)$ to the global Cartesian coordinate system. This step utilizes the exact analytical relationships, ensuring

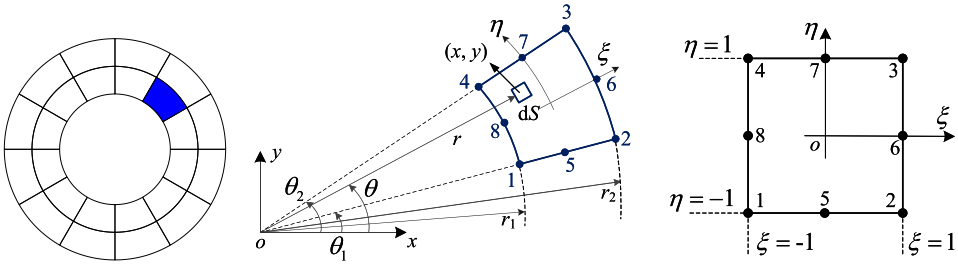

(a) (b) (c)

Fig. 1. The annular element: (a) in a mesh for a 2D ring domain; (b) polar coordinate system and (c) element natural coordinate system.

that the curvature of the annular domain is represented without geometric error:

$$\begin{cases} x(r,\theta) = r\cos\theta, \\ y(r,\theta) = r\sin\theta. \end{cases} \tag{2}$$

In the finite element implementation, the mapping from parametric coordinates (ξ,η) to physical coordinates (x,y) follows the composite path $(\xi,\eta) \to (r,\theta) \to (x,y)$. This mapping serves a dual purpose. Beyond determining the spatial location of integration points, the derivatives of the physical coordinates with respect to the parametric ones are indispensable. These derivatives constitute the Jacobian matrix, which is required to transform the gradients of shape functions from the reference domain to the physical domain for strain calculations. The evaluation of the Jacobian matrix $\mathbf{J}$ follows the chain rule, reflecting the composite nature of the geometric mapping:

$$\mathbf{J} = \begin{bmatrix} \dfrac{\partial x}{\partial \xi} & \dfrac{\partial x}{\partial \eta} \\ \dfrac{\partial y}{\partial \xi} & \dfrac{\partial y}{\partial \eta} \end{bmatrix} = \begin{bmatrix} \dfrac{\partial x}{\partial r} & \dfrac{\partial x}{\partial \theta} \\ \dfrac{\partial y}{\partial r} & \dfrac{\partial y}{\partial \theta} \end{bmatrix} \begin{bmatrix} \dfrac{\partial r}{\partial \xi} & \dfrac{\partial r}{\partial \eta} \\ \dfrac{\partial \theta}{\partial \xi} & \dfrac{\partial \theta}{\partial \eta} \end{bmatrix}. \tag{3}$$

To evaluate this explicitly, we first determine the derivatives of the intermediate coordinates with respect to the natural coordinates using (1). Let $\Delta r = r_2 - r_1$ and $\Delta\theta = \theta_2 - \theta_1$, this yields

$$\begin{bmatrix} \dfrac{\partial r}{\partial \xi} & \dfrac{\partial r}{\partial \eta} \\ \dfrac{\partial \theta}{\partial \xi} & \dfrac{\partial \theta}{\partial \eta} \end{bmatrix} = \frac{1}{2}\begin{bmatrix} \Delta r & 0 \\ 0 & \Delta\theta \end{bmatrix}. \tag{4}$$

Next, the derivatives of the Cartesian coordinates with respect to the polar coordinates are obtained from (2):

$$\begin{bmatrix} \dfrac{\partial x}{\partial r} & \dfrac{\partial x}{\partial \theta} \\ \dfrac{\partial y}{\partial r} & \dfrac{\partial y}{\partial \theta} \end{bmatrix} = \begin{bmatrix} \cos\theta & -r\sin\theta \\ \sin\theta & r\cos\theta \end{bmatrix}. \tag{5}$$

Substituting these components into the chain rule expression, the complete Jacobian matrix $\mathbf{J}$ is derived as

$$\mathbf{J} = \begin{bmatrix} \cos\theta & -r\sin\theta \\ \sin\theta & r\cos\theta \end{bmatrix} \frac{1}{2}\begin{bmatrix} \Delta r & 0 \\ 0 & \Delta\theta \end{bmatrix} = \frac{1}{2}\begin{bmatrix} \Delta r\cos\theta & -r\Delta\theta\sin\theta \\ \Delta r\sin\theta & r\Delta\theta\cos\theta \end{bmatrix}. \tag{6}$$

The determinant of the Jacobian, $J = \det\mathbf{J}$, represents the area scaling factor between the reference and physical domains and is given by

$$J = \det\mathbf{J} = \frac{1}{4}\begin{vmatrix} \Delta r\cos\theta & -r\Delta\theta\sin\theta \\ \Delta r\sin\theta & r\Delta\theta\cos\theta \end{vmatrix} = \frac{1}{4} r\Delta r\Delta\theta. \tag{7}$$

Finally, the inverse of the Jacobian matrix, denoted as $\mathbf{J}^{-1}$ (or often $\mathbf{\Gamma}$ in element formulations), is required to transform the shape function derivatives to the

Cartesian system. It is calculated as

$$\mathbf{J}^{-1} = 2 \begin{bmatrix} \dfrac{\cos\theta}{\Delta r} & \dfrac{\sin\theta}{\Delta r} \\ -\dfrac{\sin\theta}{r\Delta\theta} & \dfrac{\cos\theta}{r\Delta\theta} \end{bmatrix}. \tag{8}$$

2.1.2. *Displacement interpolation*

Let u and v be the displacement component in the x and y direction, respectively. For the displacement field, the standard interpolation is applied using the shape functions for the 8-node quadratic element:

$$\begin{bmatrix} u(\xi,\eta) \\ v(\xi,\eta) \end{bmatrix} = \sum_{i=1}^{8} N_i(\xi,\eta) \begin{bmatrix} u_i \\ v_i \end{bmatrix}, \tag{9}$$

where u_i and v_i are the nodal values of the displacement components. The eight shape functions for the Q8 element are given below for completeness:

$$\begin{aligned} N_1 &= \frac{1}{4}(1-\xi)(1-\eta)(-\xi-\eta-1), \\ N_2 &= \frac{1}{4}(1+\xi)(1-\eta)(\xi-\eta-1), \\ N_3 &= \frac{1}{4}(1+\xi)(1+\eta)(\xi+\eta-1), \\ N_4 &= \frac{1}{4}(1-\xi)(1+\eta)(-\xi+\eta-1), \\ N_5 &= \frac{1}{2}\left(1-\xi^2\right)(1-\eta), \\ N_6 &= \frac{1}{2}(1+\xi)\left(1-\eta^2\right), \\ N_7 &= \frac{1}{2}\left(1-\xi^2\right)(1+\eta), \\ N_8 &= \frac{1}{2}(1-\xi)\left(1-\eta^2\right). \end{aligned} \tag{10}$$

The spatial derivatives of the displacements, required for strain calculations, are obtained from the derivatives with respect to the natural coordinates via the chain rule:

$$\begin{bmatrix} \dfrac{\partial u}{\partial x} & \dfrac{\partial u}{\partial y} \\ \dfrac{\partial v}{\partial x} & \dfrac{\partial v}{\partial y} \end{bmatrix} = \begin{bmatrix} \dfrac{\partial u}{\partial \xi} & \dfrac{\partial u}{\partial \eta} \\ \dfrac{\partial v}{\partial \xi} & \dfrac{\partial v}{\partial \eta} \end{bmatrix} \begin{bmatrix} \dfrac{\partial \xi}{\partial x} & \dfrac{\partial \xi}{\partial y} \\ \dfrac{\partial \eta}{\partial x} & \dfrac{\partial \eta}{\partial y} \end{bmatrix}. \tag{11}$$

The coordinate transformation matrix in the above equation is defined as matrix $\mathbf{\Gamma}$, which is the inverse of the Jacobian matrix $\mathbf{J}$:

$$\mathbf{\Gamma} = \begin{bmatrix} \dfrac{\partial \xi}{\partial x} & \dfrac{\partial \xi}{\partial y} \\ \dfrac{\partial \eta}{\partial x} & \dfrac{\partial \eta}{\partial y} \end{bmatrix} = \mathbf{J}^{-1}. \tag{12}$$

2.1.3. *Element stiffness matrix*

The infinitesimal strain components are related to the nodal displacement vector $\mathbf{d} = \{u_1, v_1, \ldots, u_8, v_8\}^{\mathrm{T}}$ through the strain-displacement matrix $\mathbf{B}$. Note that the strain vector ε follows the Voigt notation constructed from the displacement gradients in (11), where γ_{xy} is the engineering shear strain:

$$\varepsilon = \begin{Bmatrix} \varepsilon_x \\ \varepsilon_y \\ \gamma_{xy} \end{Bmatrix} = \begin{Bmatrix} \dfrac{\partial u}{\partial x} \\ \dfrac{\partial v}{\partial y} \\ \dfrac{\partial u}{\partial y} + \dfrac{\partial v}{\partial x} \end{Bmatrix} = \mathbf{B}\mathbf{d}. \tag{13}$$

By combining the shape function derivatives and the geometric transformation matrix $\mathbf{\Gamma}$ derived earlier, the matrix $\mathbf{B}$ can be explicitly constructed as

$$\mathbf{B} = \begin{bmatrix} 1 & 0 & 0 & 0 \\ 0 & 0 & 0 & 1 \\ 0 & 1 & 1 & 0 \end{bmatrix} \begin{bmatrix} \mathbf{\Gamma}^{\mathrm{T}} & \mathbf{0} \\ \mathbf{0} & \mathbf{\Gamma}^{\mathrm{T}} \end{bmatrix} \begin{bmatrix} N_{1,\xi} & 0 & \cdots & N_{8,\xi} & 0 \\ N_{1,\eta} & 0 & \cdots & N_{8,\eta} & 0 \\ 0 & N_{1,\xi} & \cdots & 0 & N_{8,\xi} \\ 0 & N_{1,\eta} & \cdots & 0 & N_{8,\eta} \end{bmatrix}. \tag{14}$$

Consequently, the element stiffness matrix $\mathbf{K}$ is obtained by numerical integration over the reference domain, incorporating the Jacobian determinant J:

$$\mathbf{K} = t \int_{(x,y)} \mathbf{B}^{\mathrm{T}} \mathbf{E} \mathbf{B} \, \mathrm{d}x\mathrm{d}y = t \int_{-1}^{1} \int_{-1}^{1} \mathbf{B}^{\mathrm{T}} \mathbf{E} \mathbf{B} J \, \mathrm{d}\xi \mathrm{d}\eta, \tag{15}$$

where t denotes the element thickness, and $\mathbf{E}$ is the constitutive elasticity matrix. Depending on the stress state, $\mathbf{E}$ takes the following forms for isotropic materials (with Young's modulus E and Poisson's ratio ν):

$$\mathbf{E} = \frac{E}{1-\nu^2} \begin{bmatrix} 1 & \nu & 0 \\ \nu & 1 & 0 \\ 0 & 0 & \dfrac{1-\nu}{2} \end{bmatrix} \quad \text{(plane stress)}, \tag{16}$$

$$\mathbf{E} = \frac{E}{(1+\nu)(1-2\nu)} \begin{bmatrix} 1-\nu & \nu & 0 \\ \nu & 1-\nu & 0 \\ 0 & 0 & \dfrac{1-2\nu}{2} \end{bmatrix} \quad \text{(plane strain)}. \tag{17}$$

2.2. *Disk super element formulation*

When the annular element is used to model circular disks, which in turn are used to model particulate materials, the number of elements can be very large. To reduce the computational burden for solving large-scale models, the super element concept in the FEM [Cook *et al.* (2002)] is used next in applying the annular elements.

A 2D disk super element model is shown in Fig. 2. A super element (Fig. 2(b)) is formed based on the mesh for the circular disk using annular elements (Fig. 2(a)), with only the boundary nodes being kept in the subsequent calculation.

Let the nodal displacement vector be partitioned into boundary nodes $\mathbf{u}_\mathrm{a}$ (analysis set) and internal nodes $\mathbf{u}_\mathrm{o}$ (omitted set). By utilizing the annular element formulation described previously, the global stiffness matrix for a circular disk is assembled and partitioned to isolate the boundary DOFs:

$$\begin{bmatrix} \mathbf{K}_{\mathrm{aa}} & \mathbf{K}_{\mathrm{ao}} \\ \mathbf{K}_{\mathrm{ao}}^{\mathrm{T}} & \mathbf{K}_{\mathrm{oo}} \end{bmatrix} \begin{Bmatrix} \mathbf{u}_\mathrm{a} \\ \mathbf{u}_\mathrm{o} \end{Bmatrix} = \begin{Bmatrix} \mathbf{f}_\mathrm{a} \\ \mathbf{f}_\mathrm{o} \end{Bmatrix}. \tag{18}$$

By expanding the second row of the partitioned system, the internal displacements can be expressed in terms of the boundary displacements. This relationship, known as the recovery equation, is given by

$$\mathbf{u}_\mathrm{o} = \mathbf{K}_{\mathrm{oo}}^{-1} \left(\mathbf{f}_\mathrm{o} - \mathbf{K}_{\mathrm{ao}}^{\mathrm{T}} \mathbf{u}_\mathrm{a} \right). \tag{19}$$

Substituting (19) into the first row of the system eliminates the internal DOFs, yielding the condensed stiffness equation for the disk super element:

$$\mathbf{K}^{\mathrm{eff}} \mathbf{u}_\mathrm{a} = \mathbf{f}^{\mathrm{eff}}, \tag{20}$$

where $\mathbf{K}^{\mathrm{eff}}$ is the effective stiffness matrix (or Schur complement) associated with the boundary nodes:

$$\mathbf{K}^{\mathrm{eff}} = \mathbf{K}_{\mathrm{aa}} - \mathbf{K}_{\mathrm{ao}} \mathbf{K}_{\mathrm{oo}}^{-1} \mathbf{K}_{\mathrm{ao}}^{\mathrm{T}} \tag{21}$$

and $\mathbf{f}^{\mathrm{eff}}$ is the corresponding effective force vector:

$$\mathbf{f}^{\mathrm{eff}} = \mathbf{f}_\mathrm{a} - \mathbf{K}_{\mathrm{ao}} \mathbf{K}_{\mathrm{oo}}^{-1} \mathbf{f}_\mathrm{o}. \tag{22}$$

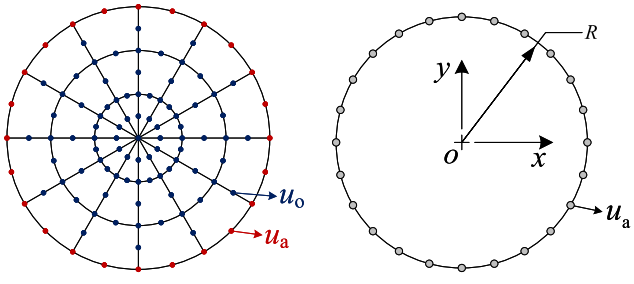

(a) (b)

Fig. 2. A disk super element model: (a) mesh on a circular disk and (b) disk super element.

This substructuring technique allows the global system to be solved initially for only the boundary nodes $\mathbf{u}_{\mathrm{a}}$. Subsequently, the internal displacements $\mathbf{u}_{\mathrm{o}}$ can be recovered for each disk individually using (19), enabling detailed stress analysis within the particulate domain.

3. Numerical Examples

To verify the new annular element formulation for solving 2D elastostatic problems, several examples are presented first, including a hollow thick-walled cylinder [Timoshenko and Goodier (1987)], a circular disk with a small circular hole [Murakami (2016)] and a solid circular disk problem [Murakami (2016)]. Then, several examples with domains represented by many solid circular disks are solved using the disk super elements. In all cases, the FEM models are applied with minimal constraints to remove the rigid-body motions.

3.1. *Examples using the annular element*

3.1.1. *A hollow thick-walled cylinder*

We first investigate the classical Lamé problem of a hollow thick-walled cylinder subjected to uniform hydrostatic pressure. The cylinder has an inner radius $a = 1.0$ and an outer radius $b = 2.0$. The problem is modeled under plane strain conditions. To eliminate rigid-body motions while allowing valid deformations, minimal constraints are applied: $u = 0$ at points B and D, and $v = 0$ at points A and C (see Fig. 3).

The general analytical solutions for the radial stress σ_r, tangential stress σ_θ, and radial displacement u_r under an internal pressure p_i and an external pressure p_o are given by Timoshenko and Goodier [1987]:

$$\begin{cases} \sigma_r(r) = -\dfrac{a^2b^2\,(p_{\mathrm{i}} - p_{\mathrm{o}})}{b^2 - a^2}\dfrac{1}{r^2} + \dfrac{a^2p_{\mathrm{i}} - b^2p_{\mathrm{o}}}{b^2 - a^2}, \\ \sigma_\theta(r) = \dfrac{a^2b^2\,(p_{\mathrm{i}} - p_{\mathrm{o}})}{b^2 - a^2}\dfrac{1}{r^2} + \dfrac{a^2p_{\mathrm{i}} - b^2p_{\mathrm{o}}}{b^2 - a^2}, \\ \tau_{r\theta} = 0 \quad \text{(axisymmetric, no shear)}, \\ u_r(r) = \dfrac{1+\nu}{E}\left[-\dfrac{a^2b^2\,(p_{\mathrm{o}} - p_{\mathrm{i}})}{b^2 - a^2}\dfrac{1}{r} + (1-2\nu)\dfrac{a^2p_{\mathrm{i}} - b^2p_{\mathrm{o}}}{b^2 - a^2}r\right]. \end{cases} \tag{23}$$

In this study, the material properties are set to Young's modulus $E = 1.0$ and Poisson's ratio $\nu = 0.3$. It is worth noting that, unlike traditional isoparametric elements where the geometry must be interpolated via shape functions, the proposed annular element possesses an analytical geometric mapping. Consequently, the coordinates and their derivatives with respect to the parameter space are computed exactly and simply, without any geometric approximation.

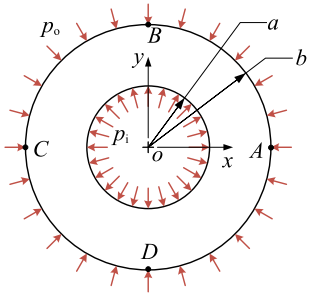

Fig. 3. Model definition for the hollow thick-walled cylinder problem.

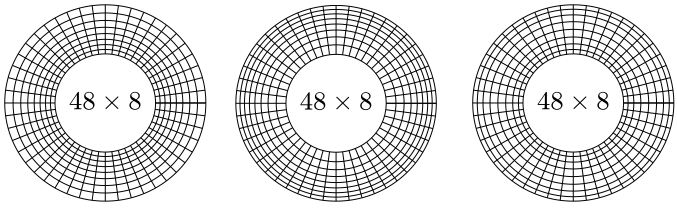

(a) (b) (c)

Fig. 4. Typical FEM mesh for the three load cases (48 × 8 mesh): (a) LC1: Dense inner; (b) LC2: Dense outer and (c) LC3: Dense B.C.

To evaluate the adaptivity of the annular element to different stress gradients, we design three load cases (LCs) with distinct mesh grading strategies, as illustrated in Fig. 4.

Load Case 1: Internal Pressure Only ($p_i = 1.0, p_o = 0$). In this case, the stress field exhibits a significant gradient near the inner boundary ($r = a$) and decays roughly as $1/r^2$ toward the outer boundary. To efficiently capture this variation, we use a graded mesh where elements are denser near the inner radius and coarser near the outer radius (Fig. 4(a)). The exact solution is

$$\begin{cases} \sigma_r = \dfrac{a^2 p_{\mathrm{i}}}{b^2 - a^2}\left(1 - \dfrac{b^2}{r^2}\right), \\ \sigma_\theta = \dfrac{a^2 p_{\mathrm{i}}}{b^2 - a^2}\left(1 + \dfrac{b^2}{r^2}\right), \\ u_r = \dfrac{1+\nu}{E}\dfrac{a^2 p_{\mathrm{i}}}{b^2 - a^2}\left[\dfrac{b^2}{r} + (1-2\nu)\, r\right]. \end{cases} \tag{24}$$

Load Case 2: External Pressure Only ($p_i = 0, p_o = 0.5$). Here, the load is applied on the outer boundary. We construct a mesh with an inverse gradient — coarser at the inner radius and denser at the outer radius (Fig. 4(b)) — to verify

the element's geometric mapping flexibility. The theoretical solution is

$$\begin{cases} \sigma_r = \dfrac{-b^2 p_{\mathrm{o}}}{b^2 - a^2}\left(1 - \dfrac{a^2}{r^2}\right), \\ \sigma_\theta = \dfrac{-b^2 p_{\mathrm{o}}}{b^2 - a^2}\left(1 + \dfrac{a^2}{r^2}\right), \\ u_r = \dfrac{1+\nu}{E}\dfrac{-b^2 p_{\mathrm{o}}}{b^2 - a^2}\left[\dfrac{a^2}{r} + (1-2\nu)\, r\right]. \end{cases} \tag{25}$$

Load Case 3: Combined Pressure ($p_i = 1.0, p_o = 0.5$). This case represents a scenario where accurate boundary information is required on both sides. We employ a bidirectional graded mesh, which is refined at both the inner and outer boundaries and coarser in the middle (Fig. 4(c)). The general analytical formulas in (23) apply directly.

Figure 3 shows the generic model definition. We performed convergence studies for all three cases using progressively refined meshes (12×2, 24×4, 48×8, 96×16, 192×32, 384×64, 768×128). To provide a fair validation, the results are compared with the standard 8-node serendipity quadrilateral element (Q8) using the exact same mesh topology. The equivalent element size h is defined as the maximum distance between any two nodes within the largest element of the mesh.

The convergence results (errors in L^2 norm and energy norm) are presented in Figs. 5–7. It can be observed that the proposed annular element (aFEM) achieves the theoretical optimal convergence rates in all three scenarios: approximately 3.0 for the L^2 norm and 2.0 for the energy norm. This rigorous convergence behavior effectively validates that the element satisfies the mathematical requirements for reliable numerical analysis. Quantitatively, the standard Q8 element exhibits slightly lower error norms. This is theoretically consistent, as the isoparametric Q8

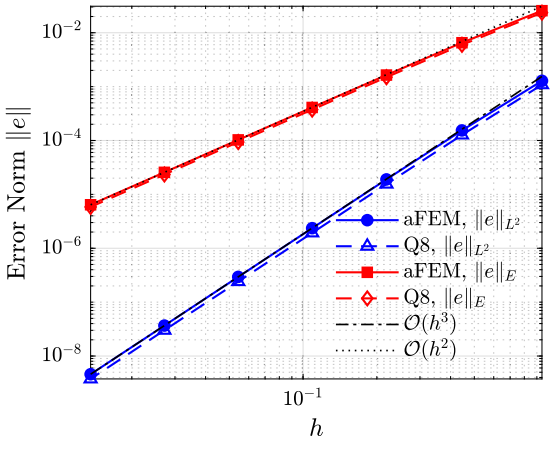

Fig. 5. Convergence of error norms for Load Case 1 ($p_i = 1$).

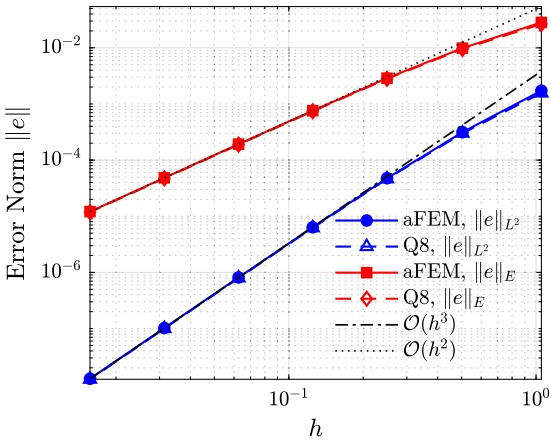

Fig. 6. Convergence of error norms for Load Case 2 ($p_o = 0.5$).

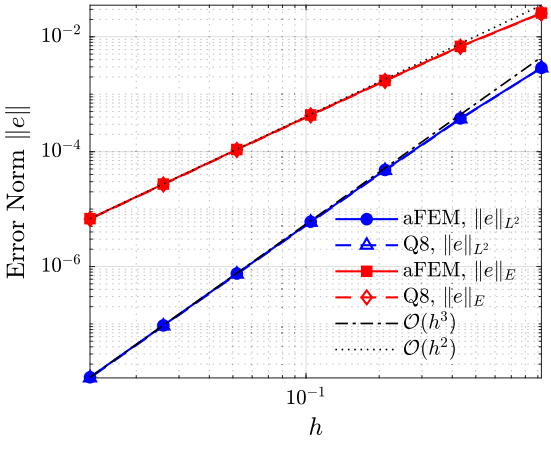

Fig. 7. Convergence of error norms for Load Case 3 ($p_i = 1, p_o = 0.5$).

mapping spans a biquadratic polynomial space, offering strong capabilities for fitting Cartesian stress gradients. However, the difference is practically negligible. Crucially, the proposed element offers a definitive advantage in geometric fidelity. Unlike the Q8 element which approximates curved boundaries via quadratic interpolation, the aFEM maintains an exact geometric representation of the circular domain. This feature is particularly advantageous for contact mechanics in particulate assemblies, where boundary smoothness is critical for accurate contact detection.

3.1.2. *A circular disk with a circular hole*

Following the verification of the proposed annular element's reliability in the previous thick-walled cylinder benchmark, we now examine its capability to capture

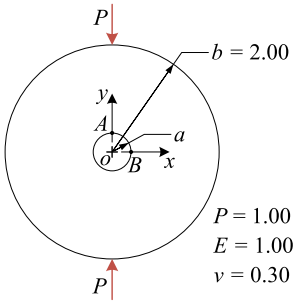

Fig. 8. A circular disk with a small circular hole subjected to concentrated compressive loads.

Table 1. Computed stress results for $d/D = 0.05 - 0.2$.

Mesh	No. of	$d/D = 0.20$		$d/D = 0.10$		$d/D = 0.05$	
	elements	σ_x (A)	σ_y (B)	σ_x (A)	σ_y (B)	σ_x (A)	σ_y (B)
12×2	24	0.69079	−1.74036	0.11220	−1.81611	−0.71152	−2.07221
24×4	96	1.20134	−1.73073	0.96597	−1.66668	0.83752	−1.61281
48×8	384	1.24654	−1.71477	1.06674	−1.68085	1.01442	−1.68156
96×16	1536	1.22761	−1.69275	1.05290	−1.65379	1.02323	−1.67459
192×32	6144	1.21589	−1.68168	1.03357	−1.62854	1.00722	−1.64367
384×64	24576	1.21131	−1.67772	1.02244	−1.61562	0.98780	−1.61699
Analytical [Murakami (2016)]		1.20926	−1.67590	1.01620	−1.60906	0.97005	−1.59632

severe stress concentrations. Specifically, a circular disk with a small central circular hole subjected to diametrical concentrated compressive loads [Murakami (2016)] is studied, as shown in Fig. 8. We assume that the diameter of the hole d $(= 2a)$ is sufficiently small compared to the diameter of the disk D $(= 2b)$, satisfying the condition $d/D \ll 1$. In this scenario, significant stress gradients occur in the immediate vicinity of the hole. Consequently, the analysis focuses on the stress accuracy at critical locations, specifically points A and B (see Fig. 8).

In this example, the domain is discretized using a series of progressively refined meshes (ranging from 12×2 to 1536×256 elements). Table 1 summarizes the computed stresses at points A and B for geometric ratios d/D varying from 0.05 to 0.2. The results demonstrate that the FEM solutions converge steadily to the analytical solutions [Murakami (2016)] as mesh density increases. Notably, high accuracy is maintained even for the extreme case of $d/D = 0.05$, validating the element's robustness in resolving highly localized stress fields.

3.1.3. *A circular disk subjected to two concentrated loads*

The circular disk subjected to a set of two opposing concentrated forces P as shown in Fig. 9 is studied next. In this case, we discretize the model into meshes with an increasing number of elements (12×3, 24×6, 48×12, 96×24, 192×48, 384×96, 768×192, 1536×384). The analytical solutions of the stress σ_x (along the y-axis)

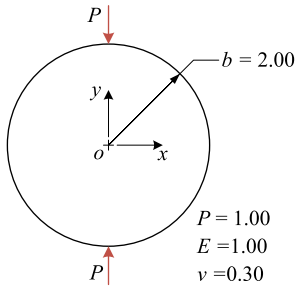

Fig. 9. A disk subjected to two concentrated forces.

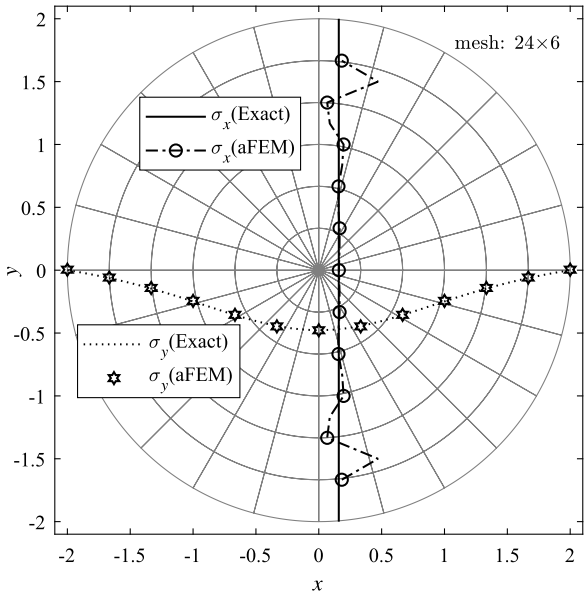

Fig. 10. Stress distributions along the x- and y-axes for the disk in Fig. 9.

and σ_y (along the x-axis) are given by Murakami [2016]:

$$\begin{cases} \sigma_x\,(0,y) = \dfrac{2P}{\pi D}, \\ \sigma_y\,(x,0) = \dfrac{2P}{\pi D}\left[1 - \dfrac{4D^4}{\left(D^2+4x^2\right)^2}\right] \end{cases} \tag{26}$$

where D is the diameter of the circular disk: $D = 2b$. It is noted that σ_x along the diameter from top to bottom (y-axis) is tensile and constant.

Figure 10 shows the stress distribution along the radial direction of the x- and y-axes on 24×6 mesh. The computed (aFEM) results of σ_y along the x-axis (where force is not directly applied) agree well with the analytical solutions, while σ_x along

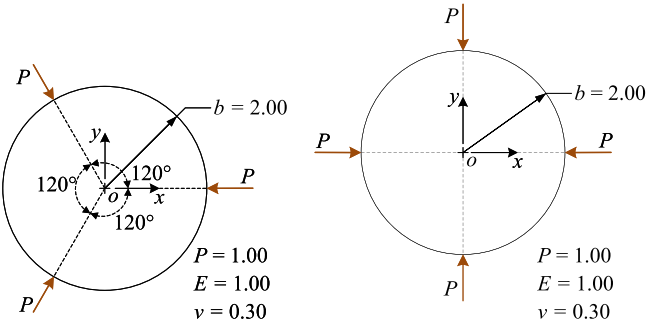

Fig. 11. A circular disk subjected to n concentrated forces: (a) $n = 3$ and (b) $n = 4$.

Table 2. Computed stresses at point O with $n = 3$ and 4.

Mesh	No. of elements	$n = 3$		$n = 4$	
		σ_x	σ_y	σ_x	σ_y
12×3	24	−0.247129	−0.247129	−0.329505	−0.329505
24×6	96	−0.239086	−0.239086	−0.318781	−0.318781
48×12	384	−0.238692	−0.238692	−0.318256	−0.318256
96×24	1536	−0.238722	−0.238722	−0.318296	−0.318296
192×48	6144	−0.238730	−0.238730	−0.318306	−0.318306
384×96	24576	−0.238732	−0.238732	−0.318309	−0.318309
Analytical solution [Murakami (2016)]		−0.238732	−0.238732	−0.318310	−0.318310

the y-axis (loading direction) can only match the analytical solution in the middle section. The stress results near the two loading points are inaccurate, due to the singularity in the solutions that cannot be captured by the FEM.

We also study the stress state at the center of the disk under various concentrated forces applied along the periphery of the disk as shown in Fig. 11. We use the same meshes (12×3, 24×6, 48×12, 96×24, 192×48, 384×96) as in the previous case. Figure 11(a) is a disk subjected to three concentrated forces, $3P$, which are loaded at an equal angle of 120° around the periphery of the disk. Similarly, Fig. 11(b) is a disk subjected to four concentrated forces with an equal angle of 90°. Generally, when n concentrated compressive forces P are loaded at equal angles around the periphery of a disk, the solutions of the stresses at the center of the disk are given by Murakami [2016]:

$$\sigma_x(0,0) = -\frac{nP}{\pi D}, \qquad \sigma_y(0,0) = -\frac{nP}{\pi D}, \qquad \tau_{xy} = 0.$$

Table 2 is a summary of the computed stress results at point O with $n = 3$ and $n = 4$. In both of the two cases, very good FEM results converging to the analytical solutions given above are obtained.

3.2. *Examples using the disk super element*

3.2.1. *Linear disk chains under concentrated forces*

In the second part of the numerical studies, we first investigate the accuracy of the disk super element using models of several disks connected in one direction. Figure 12 shows the model of two connected disks with two concentrated forces, and Fig. 14 shows the model of three connected disks with two concentrated forces. In these examples, we plot the computed stresses (see Figs. 13 and 15) along two axes by referring to the previous case (see Figs. 9 and 10) due to the similar loading condition. Similar conclusions, as in the previous case, can be drawn about the accuracy of the FEM results.

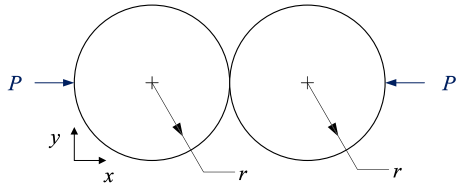

Fig. 12. Two connected disks with two concentrated forces.

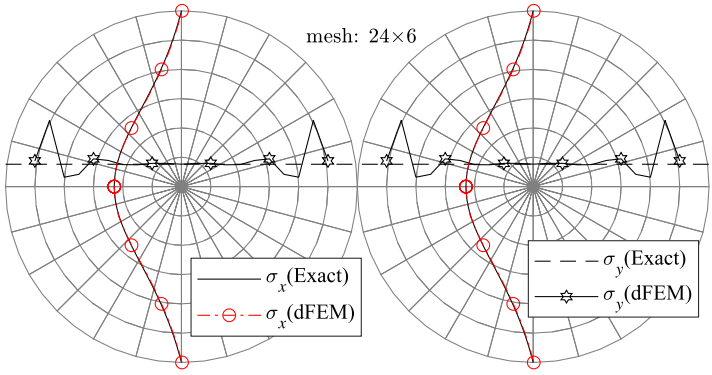

Fig. 13. Stress distributions along the x- and y-axes for the disk in Fig. 12.

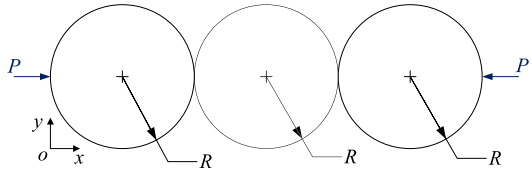

Fig. 14. Three connected disks with two concentrated forces.

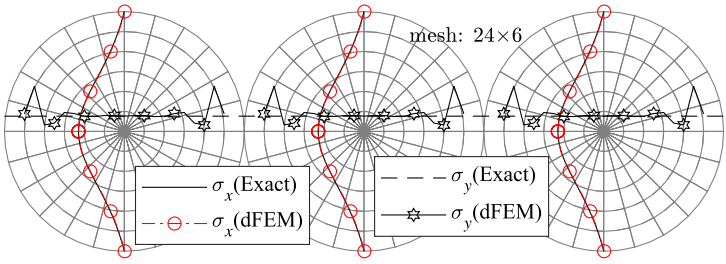

Fig. 15. Stress distributions along the x- and y-axes for the disk in Fig. 14.

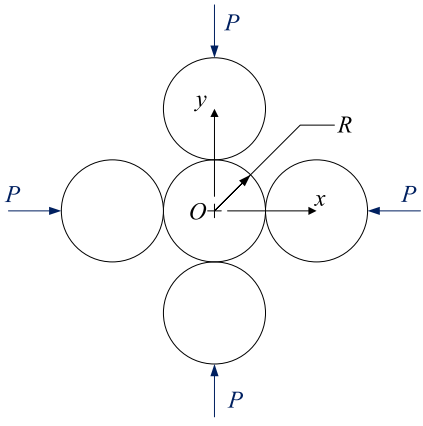

Fig. 16. Five connected disks with four concentrated forces.

3.2.2. *Planar disk clusters under centrosymmetric forces*

To further test the disk super element, we also study the case with five disks, as shown in Fig. 16. The model consists of one disk in the center, and four disks connected around the central disk at an equal angle of 90°. Figure 17 shows the comparison of the analytical solutions and FEM solutions of the stresses using the disk super element, on the diameter along the x-axis and y-axis. Similarly, the analytical solution can be found by referring to the previous case (see formulas in (26)). For the four surrounding disks, the formula of stresses is the same as (26). For the central disk, the stresses are given by adding the results in the two formulas in (26):

$$\sigma_x = \frac{2P}{\pi D}\left[2 - \frac{4D^4}{(D^2+4x^2)^2}\right], \quad \sigma_y = \frac{2P}{\pi D}\left[2 - \frac{4D^4}{(D^2+4y^2)^2}\right].$$

From Figs. 13, 15 and 17, we can find that the FEM solutions for σ_y along the x-axis (where forces are not directly applied) agree well with the analytical solution, while the FEM solutions for σ_x along the y-axis (where forces are applied) can only match the analytical solution in the middle section, due to the singularity

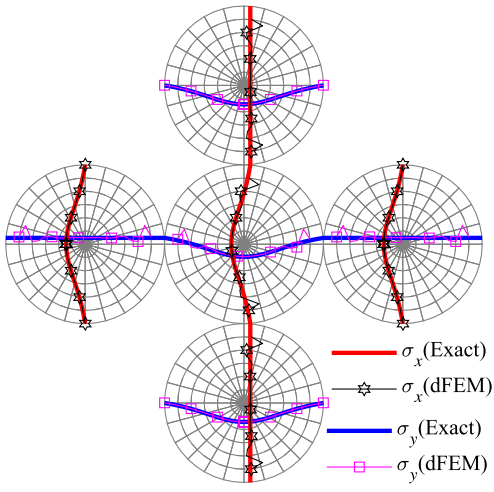

Fig. 17. Stress distributions along the x- and y-axes for the disk in Fig. 16.

in the solution. The computed stress values near the loading points are obviously inaccurate.

We also compute the case of seven disks subjected to centrosymmetric concentrated forces, as shown in Fig. 18. The model consists of one disk in the center, and six disks connected around the central disk at an equal angle of 60°. Since the case does not have reference solutions, we only provide the contour plots of computed stresses (see Fig. 19). Stress concentration is observed near the six loading points and all contact points, and the stress contour plots are consistent with the expected symmetry patterns.

3.2.3. *Disk packing in a 2D domain*

To further apply our disk super element, we use disks to fill a 2D domain, as shown in Fig. 20. The left end of the domain is fixed and the right end is subjected to a uniform pressure loading. Figure 21 shows the same sized plate filled with disks of different radius, in which, R represents the radius of all disks and m represents the number of disk super elements. Obviously, we can set the diameter of the disk as small as possible to fully fill the 2D domain. In this simulation, each disk is discretized using a uniform 24×6 mesh (24 elements in the circumferential direction and 6 elements in the radial direction), consistent with the discretization employed in the preceding examples (see Secs. 3.2.1 and 3.2.2). This mesh density is selected based on the convergence study in Sec. 3.1.3 (the disk subjected to concentrated loads), which demonstrated that a 24×6 mesh provides a sufficiently converged solution for the internal stress field.

Figures 22–25 show the contour plots of the computed stress and displacement fields with the same sized domain, but with disks of two different radii. The two

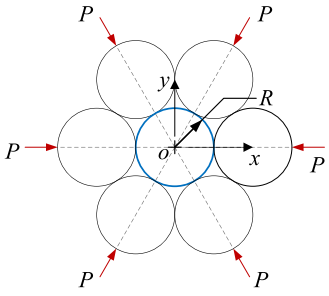

Fig. 18. Seven disks with centrosymmetric concentrated forces.

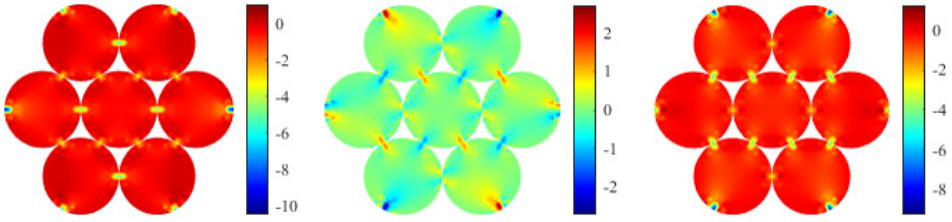

(a) (b) (c)

Fig. 19. Contour plots of computed stresses of the seven disks model: (a) σ_x; (b) σ_y and (c) τ_{xy}.

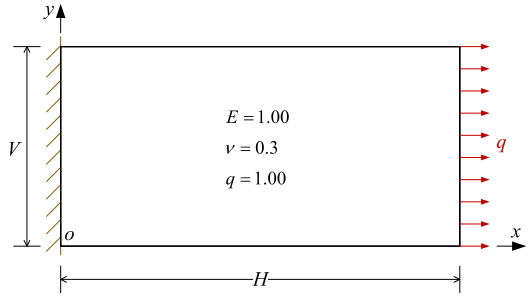

Fig. 20. A 2D domain to be modeled with disk super elements.

cases practically show the same distributions of the stress and displacement fields. It is worth mentioning that for the second case in Figs. 24 and 25, the FEM model includes about 5000 disks (or super elements), and the model can be solved on a desktop PC within 20 min.

To quantitatively demonstrate the computational advantages and physical consistency of the proposed method in large-scale simulations, we analyzed the problem using seven different disk radii ranging from $R = 1.0$ down to $R = 0.1$. The results are summarized in Figs. 26 and 27.

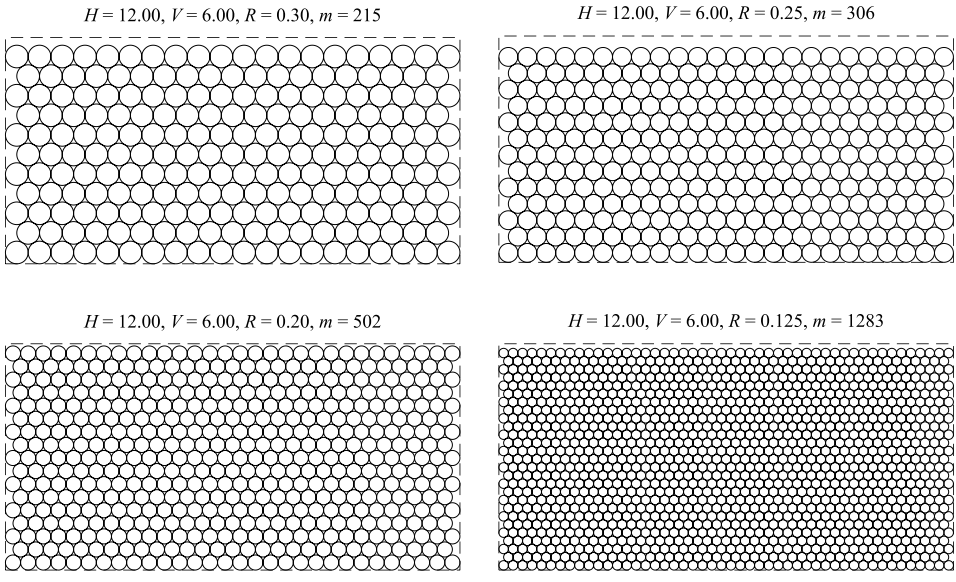

Fig. 21. The domain filled with disks.

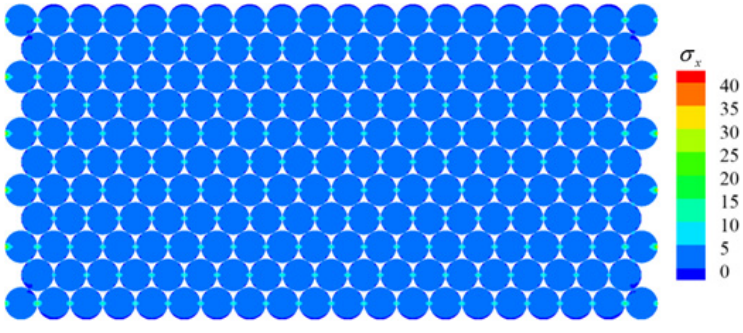

Fig. 22. Contour plot of computed σ_x on 2D plate with $H = 12.00$, $V = 6.00$, $R = 0.30$, $m = 215$.

Figure 26 illustrates the computational efficiency. As the number of disks m increases to 2023 ($R = 0.1$), the total DOFs of the full system reaches approximately 1,752,000. However, by employing the proposed super element with static condensation, the active DOFs involved in the global system of equations are reduced to only 194,208a reduction factor of approximately 9. Consequently, the total computational time for this million-DOF problem demonstrates high efficiency, requiring only about 90 s on a standard desktop PC. This duration encompasses the entire simulation pipeline, including mesh generation, file I/O, system assembly, solution and post-processing (contour plotting). This confirms the significant efficiency advantage of the proposed method for large-scale granular-like assemblies.

Figure 27 presents the convergence of macroscopic properties. Due to the boundary effect, the packing density η is lower when the number of disks m is

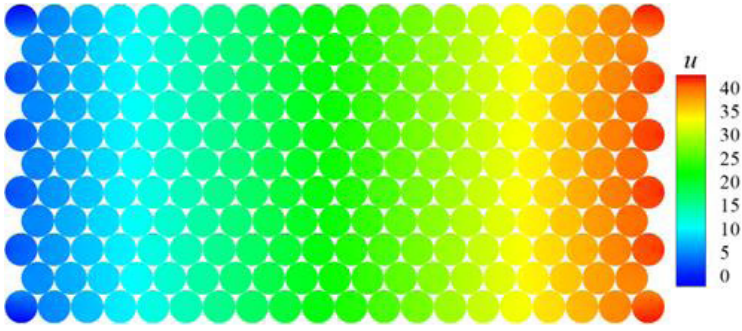

Fig. 23. Contour plot of computed displacement u on 2D plate with $H = 12.00$, $V = 6.00$, $R = 0.30$, $m = 215$.

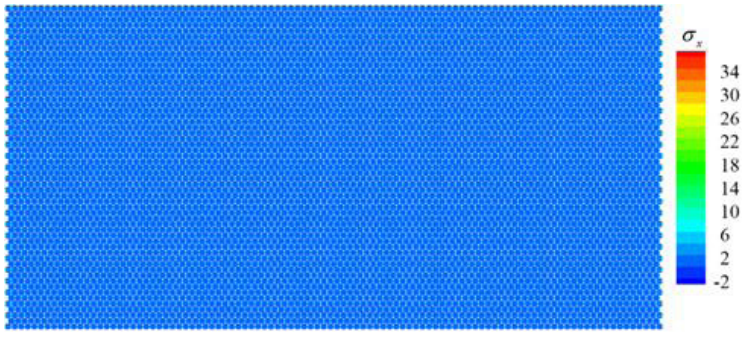

Fig. 24. Contour plot of computed σ_x on 2D plate with $H = 12.00$, $V = 6.00$, $R = 0.06$, $m = 5672$.

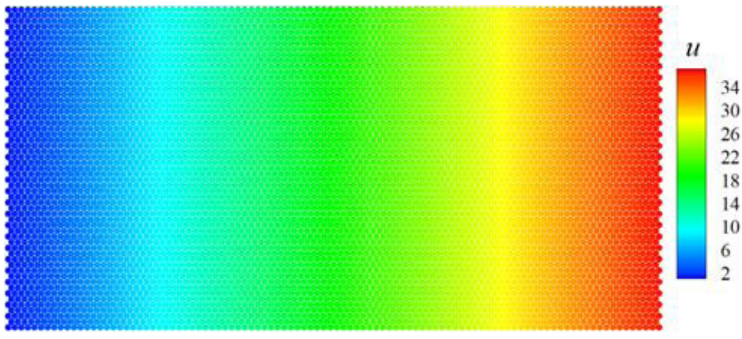

Fig. 25. Contour plot of computed displacement u on 2D plate with $H = 12.00$, $V = 6.00$, $R = 0.06$, $m = 5672$.

small, resulting in a lower effective stiffness. As the radius decreases and the number of disks m increases, η gradually converges toward the theoretical maximum for hexagonal packing (constrained by the boundary shape) and the calculated effective Young's modulus E_{eff} stabilizes at approximately 0.317. It is important to clarify

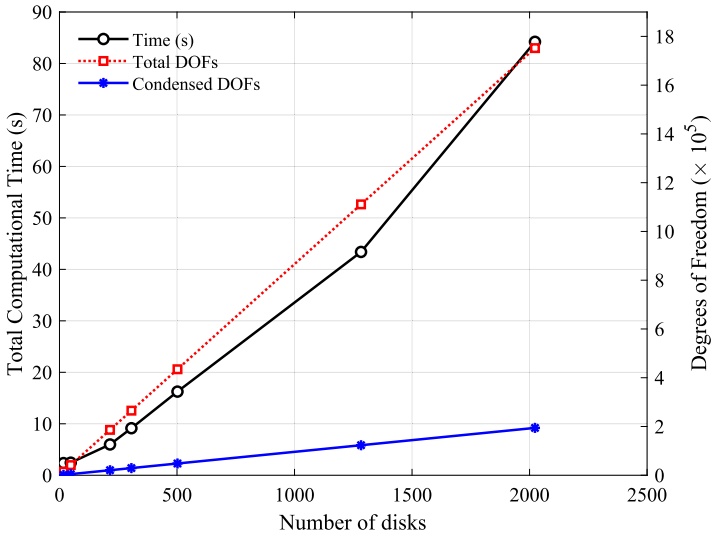

Fig. 26. Computational efficiency showing time cost and DOF reduction with different number of disks (from 17 to 2023).

that this effective stiffness is naturally lower than the Young's modulus of the constituent solid material ($E = 1.0$). This reduction is physically evident because the domain is not a solid continuum but a porous assembly of disks. The potential for deformation is higher due to the voids and the discrete load transmission pathways inherent in the hexagonal packing structure. This convergence behavior verifies the method's capability to correctly capture the homogenization process of particulate composites. In the case of disk packing, the disks are connected by the consistency of displacement at the tangent point (contact point), so that the displacement and stress can be transmitted, and the system matrix is guaranteed to be positive definite.

4. Discussions and Conclusions

A new annular finite element and a circular disk super element have been developed for solving 2D elastostatic problems involving circular domains. The annular element employs an analytical geometric mapping based on polar coordinates, so that the geometry and its Jacobian are computed exactly, eliminating the geometric discretization errors inherent in standard isoparametric elements. The displacement field uses the standard 8-node serendipity (Q8) shape functions, maintaining compatibility with the conventional finite element framework.

The element formulation has been verified through a systematic sequence of benchmark problems. The convergence study on the thick-walled cylinder problem confirms that the annular element achieves the theoretical optimal convergence rates (approximately 3.0 in the L^2 norm and 2.0 in the energy norm), consistent with

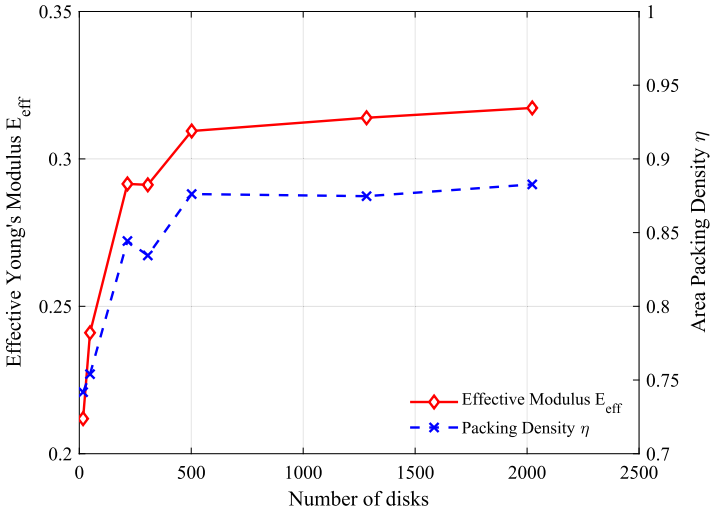

Fig. 27. Convergence of effective Young's modulus E_{eff} and packing density η with increasing number of disks.

those of the standard Q8 element. Although the Q8 element exhibits marginally lower error norms due to the richer biquadratic polynomial space of its isoparametric mapping, the proposed element offers a definitive advantage in geometric fidelity — an essential feature for contact mechanics in particulate assemblies. The stress concentration analysis of a disk with a small hole and the disk under concentrated loads further demonstrate the element's capability to resolve severe stress gradients and its expected behavior near point-load singularities.

By applying the substructuring (static condensation) technique, the disk super element condenses the internal DOFs, significantly reducing the size of the global system. For the large-scale disk packing simulation with 2023 disks, the active DOFs are reduced by a factor of approximately 9 (from 1,752,000 to 194,208), and the entire simulation pipeline completes within 90 s on a standard desktop PC. The disk packing results also show that the effective Young's modulus converges as the number of disks increases, verifying the method's capability to capture the homogenization behavior of particulate composites.

Several limitations of the current work should be noted. First, the present formulation is restricted to linear elasticity under plane stress or plane strain conditions. Second, the disk packing examples employ an idealized hexagonal close-packing arrangement with single-point tangential contact between disks. In realistic granular materials and composites, the packing configurations are generally irregular and random, involving varying particle sizes, nonuniform contact conditions and possible gaps or overlaps. Third, the stress field near concentrated forces or contact points exhibits singularities that cannot be fully resolved by the standard polynomial interpolation used in this work.

Several directions for future research are envisioned. First, the method can be extended to handle more general and realistic packing configurations, including random packings with varying disk sizes and nontangential contact conditions. Second, the displacement interpolation can be enriched to better capture the singular stress fields near concentrated forces and contact points. Third, nonlinear material models can be incorporated to account for local plastic deformation and damage, broadening the applicability to inelastic contact problems. Finally, extending the formulation to 3D spherical elements remains a challenging but practically important direction for modeling real particulate composites and microstructures.

References

Beirão da Veiga, L., Russo, A. and Vacca, G. [2019] "The virtual element method with curved edges," *ESAIM: Math. Model. Numer. Anal.* **53**(2), 375–404, doi: 10.1051/m2an/2018048.

Chen, H., Sun, Y., Yuan, W., Pang, S., Yan, W. and Shi, Y. [2022] "A review on discrete element method simulation in laser powder bed fusion additive manufacturing," *Chin. J. Mech. Eng.: Addit. Manuf. Front.* **1**(1), 100017, doi: 10.1016/j.cjmeam.2022.100017.

Chi, H. and Paulino, G. H. [2019] "Isogeometric polygonal finite element method for optimization of flows in porous media," *J. Comput. Phys.* **393**, 1–31.

Cook, R. D., Malkus, D. S., Plesha, M. E. and Witt, R. J. [2002] *Concepts and Applications of Finite Element Analysis*, 4th edition (John Wiley & Sons, New York).

Fransen, M., Fürst, A., Tunuguntla, D., Wilke, D. N., Alkin, B., Barreto, D., Brandstetter, J., Cabrera, M. A., Fan, X., Guo, M., Kieskamp, B., Kumar, K., Morrissey, J., Nuttall, J., Ooi, J., Orozco, L., Papanicolopulos, S.-A., Qu, T., Schott, D., Shuku, T., Sun, W., Weinhart, T., Ye, D. and Cheng, H. [2026] "Towards scientific machine learning for granular material simulations: Challenges and opportunities," *Arch. Comput. Methods Eng.* **33**(1), 789–821, doi: 10.1007/s11831-025-10322-8.

Giovine, P., Kyriakides, S., Mariano, P. M., Mortara, G. and di Prisco, C. [2020] "Micromechanics of granular matter," *Int. J. Solids Struct.* **187**, 1–162, doi: 10.1016/j.ijsolstr.2019.11.001.

Guarino, G., Antolin, P., Milazzo, A. and Buffa, A. [2024] "An interior penalty coupling strategy for isogeometric non-conformal Kirchhoff–Love shell patches," *Eng. Comput.* **40**(5), 3031–3057.

Jonsson, T., Larson, M. G. and Larsson, K. [2025] "Robust trimmed multipatch IGA with singular maps," *Comput. Methods Appl. Mech. Eng.* **444**, 118124.

Liu, X., Wang, Q., Wang, Y. and Dong, Q. [2023] "Review of calibration strategies for discrete element model in quasi-static elastic deformation," *Sci. Rep.* **13**(1), 13264, doi: 10.1038/s41598-023-39446-2.

Liu, Y., Sun, W., Yuan, Z. and Fish, J. [2021] "Finite element modeling of granular materials with a particle-to-element ratio close to one," *Comput. Geotech.* **136**, 104192.

Marussig, B. and Hughes, T. J. R. [2018] "A review of trimming in isogeometric analysis: Challenges, data exchange and simulation aspects," *Comput. Methods Appl. Mech. Eng.* **328**, 498–559, doi: 10.1016/j.cma.2017.09.022.

Mathews, A., Cheng, H., Celigueta, M. A., Papanicolopulos, S.-A. and Ooi, J. Y. [2026] "Concurrent multi-scale modeling of granular materials: Benchmarking volume-coupled DEM-FEM models across elastic and elasto-plastic regimes," *Comput. Geotech.* **191**, 107834, doi: 10.1016/j.compgeo.2025.107834.

Murakami, Y. [2016] *Theory of Elasticity and Stress Concentration* (John Wiley & Sons), doi: 10.1002/9781119274482.

Ngo, T. D., Kashani, A., Imbalzano, G., Nguyen, K. T. and Hui, D. [2018] "Additive manufacturing (3D printing): A review of materials, methods, applications and challenges," *Compos. B, Eng.* **143**, 172–196, doi: 10.1016/j.compositesb.2018.02.012.

Olson, M. D. and Lindberg, G. M. [1970] "Annular and circular sector finite elements for plate bending," *Int. J. Mech. Sci.* **12**(1), 17–33, doi: 10.1016/0020-7403(70)90060-6.

Ooi, E. T., Song, C. and Natarajan, S. [2018] "Polygon scaled boundary finite element formulation for topology optimization of fluid–structure interaction problems," *Int. J. Numer. Methods Eng.* **114**(5), 522–546, doi: 10.1002/nme.5760.

Raju, I. S., Krishnamurty, A. V. and Rao, A. K. [1973] "Sector elements for matrix displacement analysis," *Int. J. Numer. Methods Eng.* **6**(4), 553–563, doi: 10.1002/nme.1620060411.

Raju, I. S. and Rao, A. K. [1969] "Stiffness matrices for sector elements," *AIAA J.* **7**(1), 156–157, doi: 10.2514/3.5048.

Rao, M. N. B., Guruswamy, P. and Sampathkumaran, K. S. [1977] "Finite element analysis of thick annular and sector plates," *Nucl. Eng. Des.* **41**(2), 247–255, doi: 10.1016/0029-5493(77)90096-7.

Reichle, M., Arf, J., Simeon, B. and Klinkel, S. [2023] "Smooth multi-patch scaled boundary isogeometric analysis for Kirchhoff–Love shells," *Comput. Methods Appl. Mech. Eng.*

Sawko, F. and Merriman, P. A. [1971] "An annular segment finite element for plate bending," *Int. J. Numer. Methods Eng.* **3**(1), 119–129, doi: 10.1002/nme.1620030109.

Sevilla, R. and Huerta, A. [2018] "3D NURBS-enhanced finite element method for elastostatics," *Int. J. Numer. Methods Eng.* **113**(9), 1541–1563, doi: 10.1002/nme.5707.

Singh, S. and Ramaswamy, G. S. [1972] "A sector element for thin plate flexure," *Int. J. Numer. Methods Eng.* **4**(1), 133–142, doi: 10.1002/nme.1620040111.

Stephenson, K. [2003] "Circle packing: A mathematical tale," *Not. Am. Math. Soc.* **50**(11), 1376–1388.

Timoshenko, S. P. and Goodier, J. N. [1987] *Theory of Elasticity*, 3rd edition (McGraw-Hill, New York).

Wang, Y., Zhang, H. and Xu, Y. [2018] "Finite element analysis of particle reinforced composites with interface damage," *Compos. Struct.* **202**, 183–189.

Wilson, G. J. and Kirkhope, J. [1976] "Finite element bending analysis of nonuniform circular plates," *Comput. Struct.* **6**(6), 459–466, doi: 10.1016/0045-7949(76)90041-3.

Xu, G., Li, M., Mourrain, B., Rabczuk, T., Brivadis, L. and Jüttler, B. [2018] "Parameterization of computational domain for isogeometric analysis: A survey," *Comput. Methods Appl. Mech. Eng.* **329**, 263–299, doi: 10.1016/j.cma.2017.09.027.

Yuan, X., Zhang, Y., Chen, Y., Qu, X., Yin, H., Yan, Z., Feng, Z. and Tan, Z. [2025] "Study of 3D MPFEM simulation for high-velocity compaction of 2024 Al alloy powders," *Sci. Rep.* **15**(1), 31305, doi: 10.1038/s41598-025-17353-y.

Zhang, H. and Wang, X. [2019] "A review of mechanics of particle reinforced composites," *Compos. Struct.* **209**, 786–798.

Zhao, J. [2020] "Multiscale modeling of granular media: A review," *Acta Geotech.* **15**, 1–25.